Perez, J. P. H., Tobler, D. J., Thomas, A. N., Freeman, H., Dideriksen, K., Radnik, J., Benning, L. G. (2019): Adsorption and Reduction of Arsenate during the Fe2+ -Induced Transformation of Ferrihydrite. - *ACS Earth Space Chemistry*, *3*, 6, pp. 884—894.

DOI: http://doi.org/10.1021/acsearthspacechem.9b00031

ACS EARTH AND SPACE CHEMISTRY

Article

Cite This: ACS Earth Space Chem. 2019, 3, 884–894

http://pubs.acs.org/journal/aesccq

Adsorption and Reduction of Arsenate during the Fe^{2+}-Induced Transformation of Ferrihydrite

Jeffrey Paulo H. Perez,*[,†,‡] Dominique J. Tobler,[§] Andrew N. Thomas,[∥] Helen M. Freeman,[†,#] Knud Dideriksen,[§,¶] Jörg Radnik,[⊥] and Liane G. Benning[†,‡,Δ]

[†]GFZ German Research Center for Geosciences, Telegrafenberg, 14473 Potsdam, Germany

[‡]Department of Earth Sciences, Free University of Berlin, 12249 Berlin, Germany

[§]Nano-Science Center, Department of Chemistry, University of Copenhagen, 2100 Copenhagen, Denmark

[∥]Institute of Applied Geosciences, Karlsruhe Institute of Technology, 76137 Karlsruhe, Germany

[#]School of Chemical and Process Engineering, University of Leeds, Leeds LS2 9JT, United Kingdom

[¶]Geological Survey of Denmark and Greenland (GEUS), 1350 Copenhagen K, Denmark

[⊥]Federal Institute for Materials Research and Testing (BAM), 12205 Berlin, Germany

[Δ]School of Earth and Environment, University of Leeds, Leeds LS2 9JT, United Kingdom

Supporting Information

ABSTRACT: Iron (oxyhydr)oxides play an important role in controlling the mobility and toxicity of arsenic (As) in contaminated soils and groundwaters. Dynamic changes in subsurface geochemical conditions can impact As sequestration and remobilization since the fate of As is highly dependent on the dominant iron mineral phases present and, specifically, the pathways through which these form or transform. To assess the fate of arsenate [As(V)] in subsurface settings, we have investigated the Fe^{2+}-induced transformation of As(V)-bearing ferrihydrite (As(V)-FH) to more crystalline phases under environmentally relevant anoxic subsurface conditions. Specifically, we examined the influence of varying $Fe^{2+}_{(aq)}/Fe(III)_{solid}$ ratios (0.5, 1, 2) on the behavior and speciation of mineral-bound As species during the transformation of As(V)-FH to crystalline iron-bearing phases at circumneutral pH conditions. At all $Fe^{2+}_{(aq)}/Fe(III)_{solid}$ ratios, goethite (GT), green rust sulfate (GR_{SO4}), and lepidocrocite (LP) formed within the first 2 h of reaction. At low ratios (0.5 to 1), initially formed GR_{SO4} and/or LP dissolved as the reaction progressed, and only GT and some unreacted FH remained after 24 h. At $Fe^{2+}_{(aq)}/Fe(III)_{solid}$ ratio of 2, GR_{SO4} remained stable throughout the 24 h of reaction, alongside GT and unreacted As(V)-FH. Despite the fact that majority of the starting As(V)-FH transformed to other phases, the initially adsorbed As was not released into solution during the transformation reactions, and ~99.9% of it remained mineral-bound. Nevertheless, the initial As(V) became partially reduced to As(III), most likely because of the surface-associated Fe^{2+}-GT redox couple. The extent of As(V) reduction increased from ~34% to ~40%, as the $Fe^{2+}_{(aq)}/Fe(III)_{solid}$ ratio increased from 0.5 to 2. Overall, our results provide important insights into transformation pathways of iron (oxyhydr)oxide minerals in As contaminated, anoxic soils and sediments and demonstrate the impact that such transformations can have on As mobility and also importantly oxidation state and, hence, toxicity in these environments.

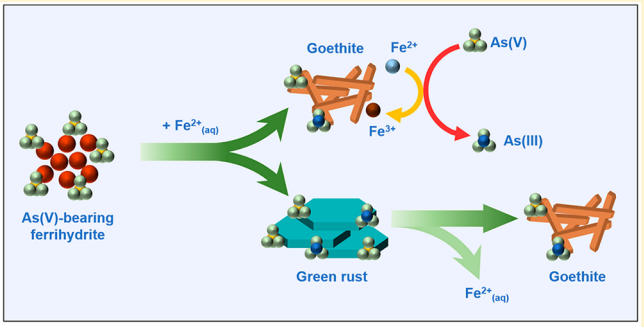

KEYWORDS: *arsenic, ferrihydrite, goethite, green rust, mineral transformation, XAS, XPS*

INTRODUCTION

Ferrihydrite (FH) is a nanoparticulate ferric oxyhydroxide mineral commonly found in natural and engineered environments (e.g., soils, groundwater, acid mine drainage, and acid sulfate soils).[1,2] FH can sequester considerable amounts of trace or toxic elements via adsorption or coprecipitation due to its high specific surface area (from 120 to 850 $m^2\ g^{-1}$) and reactivity.[3−8] However, FH is thermodynamically metastable and usually transforms to more crystalline iron (oxyhydr)-oxides (e.g., goethite, hematite, lepidocrocite, green rust, or magnetite),[1] whereby any adsorbed or incorporated compounds can be remobilized and redistributed. FH transformation in oxic, ambient conditions and at circumneutral pH

Special Issue: Iron Redox Chemistry and Its Environmental Impact

Received: February 12, 2019
Revised: April 23, 2019
Accepted: April 25, 2019
Published: April 25, 2019

is very slow (months to years),[9] and the rates, mechanisms, and pathways of transformation strongly depend on physicochemical factors including pH,[10−12] temperature,[11,12] and the presence of inorganic ions[4,12−14] and organic ligands.[15,16]

In anoxic and nonsulfidic environments, FH transformations can occur more rapidly (within hours or days) due to the presence of aqueous ferrous iron ($Fe^{2+}_{(aq)}$),[17−20] generated by dissimilatory iron-reducing bacteria.[21,22] FH transformation usually starts by an initial adsorption of aqueous Fe^{2+} onto FH surface sites and the oxidation of this surface-bound Fe(II) to surface Fe(III) species by loss of an electron to the FH solid. This electron is then conducted through the FH and eventually leads to a release of $Fe^{2+}_{(aq)}$.[23−26] This electron conduction process creates "reactive" surface sites, which in turn initiates the dissolution of FH and recrystallization to goethite (GT) and/or lepidocrocite (LP).[17,27] If the aqueous Fe^{2+} is in excess compared to the solid Fe(III) (oxyhydr)oxide (e.g., FH, GT, and LP), it can transform to mixed-valent Fe minerals such as green rust (GR) and magnetite (MGT).[28−30] Hence, FH transformations can lead to a variety of Fe mineral phases, and each of these phases has different sorption and redox properties. In turn, this will affect biogeochemical cycling of iron and nutrients[21] and importantly also the sequestration of FH-bound toxic elements.

Arsenic is a persistent contaminant affecting groundwater resources worldwide due to its widespread occurrence and distribution.[31,32] Its mobility in the environment can be greatly influenced by its interaction with mineral phases such as iron (oxhydr)oxides, which have been shown to be highly effective substrates for the sequestration of As in contaminated groundwater. However, the adsorption capacity of iron (oxyhydr)oxides varies dramatically and is also strongly affected by the As oxidation state, which can quickly change during Fe redox transformations. Among the various iron (oxyhydr)oxides, FH, which is often the first Fe phase forming in subsurface near-neutral environments, exhibits one of the highest adsorption affinities for both As(III) and As(V) , while most crystalline Fe phases have far lower As adsorption affinities.[33−38] Under anoxic conditions and in the presence of $Fe^{2+}_{(aq)}$, FH readily transforms to crystalline Fe phases, and this can be accompanied by the release and remobilization of As back into the aqueous phase or the As can become associated with the newly formed Fe phases. However, the mechanisms and pathways of these processes during the intertransformation of the various iron (oxyhydr)oxides is, however, so far poorly understood or quantified.

To the best of our knowledge, only a few studies examined the Fe^{2+}-induced transformation of As-bearing FH under anoxic conditions. Pedersen et al.[39] used ^{55}Fe and ^{73}As radiotracers to monitor the transformation of As(V)-coprecipitated FH at pH 6.5 and at varying $Fe^{2+}_{(aq)}$ concentrations (0 to 1 mM), an $Fe(III)_{FH}$ loading of 0.5 mM, and As/Fe_{solid} ratios between 0.001 to 0.005. They showed that after 5 days, LP and GT formed at low $[Fe^{2+}_{(aq)}]$, while GT and MGT formed at higher $[Fe^{2+}_{(aq)}]$. They also inferred that the coprecipitated As had little to no effect on the FH transformation rates and that most of the As remained associated with the solids. More recently, Masue-Slowey et al.[40] investigated the Fe^{2+}-induced transformation of As(V)-adsorbed FH. They used higher As/Fe_{solid} ratios (0.013 to 0.05), higher $Fe(III)_{FH}$ loadings (20 mM), and also up to 2 mM of $Fe^{2+}_{(aq)}$ concentration. They showed that LP and MGT formed instead of GT, and that the preadsorbed As retarded FH transformation. These studies have provided insights into the mineralogical changes that occur when As-bearing FH is reacted with varying $[Fe^{2+}_{(aq)}]$ and revealed how the transformation rates can be affected by the presence of As. However, the fate, bonding environment, or redox state of the coprecipitated or adsorbed As during the crystallizations remains elusive. The questions of whether transformation reactions in systems where higher amounts of As are associated with the initial FH will cause As release, and what happens if As is only adsorbed to FH rather than coprecipitated are still open. Moreover, As oxidation state could be affected by these redox reactions, and this would affect the toxicity of As in the subsurface. Lastly, the previously tested conditions do not favor GR formation; however, GR phases may be a key substrate for As sequestration in Fe-rich and oxygen-poor subsurface environments (e.g., gley soils or contaminated aquifers), particularly as they can adsorb large amounts of As.[33,41] Thus, GR formation, stability, and behavior with respect to As has to be evaluated.

Herein, we aim to fill a part of this knowledge gap by describing a study in which we performed batch experiments under anoxic conditions and examined the Fe^{2+}-induced transformation of As(V)-bearing FH. Experiments were carried out at pH 6.5 with FH onto which As(V) was adsorbed and was subsequently reacted at varying $Fe^{2+}_{(aq)}/Fe(III)_{solid}$ ratios for up to 24 h. In particular, we tested $Fe^{2+}_{(aq)}/Fe(III)_{solid}$ concentrations and ratios that were higher than in the above-mentioned studies but that have been shown to favor the formation of GR.[29,41] The mineralogical transformations of As(V)-FH and the fate of As in these processes were assessed using conventional laboratory and synchrotron-based X-ray scattering and spectroscopic techniques, and the resulting products were imaged using electron microscopy. Our results provide new insights on the influence of iron (oxyhydr)oxide mineral transformations on the speciation and hence mobility and toxicity of As in contaminated subsurface environments.

EXPERIMENTAL SECTION

General Methods. All glass- and plastic-wares were cleaned in 5 M HCl for 24 h, followed by thorough rinsing with Milli-Q water (~18.2 MΩ·cm). All chemicals were ACS reagent grade from Sigma-Aldrich and Acros Organics and were used as received. Stock solutions were prepared inside the anaerobic chamber (97% N_2, 3% H_2, Coy Laboratory Products, Inc.) using O_2-free water, which was obtained by purging Milli-Q water with O_2-free nitrogen for at least 4 h.

Synthesis of Two-Line FH. Two-line FH was synthesized using the method described by Schwertmann and Cornell[42] by slowly titrating 0.1 M $Fe_2(SO_4)_3{\cdot}5H_2O$ with 1 M NaOH to pH ≈ 7. The resulting suspension was washed using six cycles of centrifugation (9000 rpm, 5 min) and redispersion in Milli-Q water to remove excess solutes. Afterward, the FH slurry was purged with O_2-free N_2 for at least 4 h to remove O_2 and then immediately transferred into the anaerobic chamber. The amount of synthesized FH was determined based on the total iron concentration of an aliquot of the suspension dissolved in 0.3 M HNO_3. The total Fe concentration was analyzed by flame atomic absorption spectrometry (AAS, PerkinElmer AAS Analyst 800). Each batch of FH (~88.3 mM $Fe(III)_{solid}$) was prepared fresh and used on the day of synthesis.

Batch Transformation Experiments. All batch experiments were performed in triplicate at room temperature inside

DOI: 10.1021/acsearthspacechem.9b00031
ACS Earth Space Chem. 2019, 3, 884−894

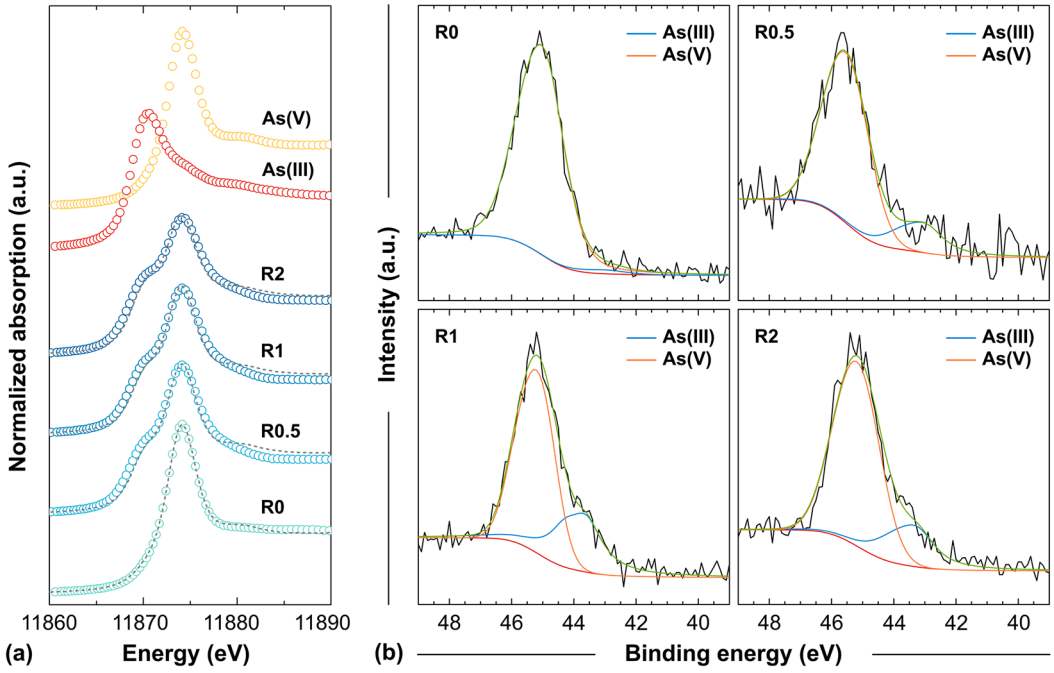

Figure 1. (a) Normalized As K-edge XANES spectra of the end-products. Fits (gray dashed lines) are linear combinations of the As reference standards (i.e., As(III) and As(V) adsorbed on GT). (b) Deconvoluted high-resolution As 3d XPS spectra of the end-products (calibrated to yield adventitious C 1s peak at 285.0 eV). Details of the fitting parameters and statistics for the quantification of As speciation based from the As K-edge XANES and XPS data can be found in Tables S-2 and S-4, respectively.

the anaerobic chamber. To prepare As(V)-bearing FH, an aliquot of the washed FH was resuspended in a 0.1 M NaCl solution buffered at pH 6.5 using 0.05 M morpholinoethanesulfonic acid (MOPS). After pH equilibration, the resulting FH suspension was then spiked with an aliquot from an As(V) stock solution prepared from $Na_2HAsO_4{\cdot}7H_2O$. The resulting suspensions [41.6 mM $Fe(III)_{solid}$, 1.33 mM As(V)] were stirred at 350 rpm for 24 h to ensure As(V) adsorption onto FH (Figure S-1). Afterward, aliquots of 0.5 M $FeSO_4$ were added to the As(V)-bearing FH suspension to achieve $Fe^{2+}_{(aq)}$/$Fe(III)_{solid}$ ratios of 0.5, 1, or 2 (denoted as R0.5, R1, and R2 from here on). A control experiment without $FeSO_4$ addition (no aqueous Fe^{2+}, R0) was also conducted. The resulting mixtures were stirred at 350 rpm for 24 h, with aliquots of the suspension being removed after 0.5, 1, 2, 4, 8, and 24 h. Parts of the collected suspensions were filtered through 0.22 μm syringe filters, and the resulting solutions were acidified with HNO_3 and stored at 4 °C until the concentrations of aqueous As were analyzed by inductively coupled plasma optical emission spectrometry (ICP-OES, Varian 720ES), following the method described by Perez et al.[33] Further analytical details can be found in the Supporting Information (Text S-1, Table S-1). The remainder of the collected suspensions was used to characterize the solid phase. For this, the suspension was filtered using 0.22 μm polycarbonate membrane filters, and the obtained solids were dried in a desiccator inside the chamber, ground, and stored until use in crimped headspace vials inside the anaerobic chamber.

Mineral Characterization and Thermodynamic Modeling. The solids were analyzed by a suite of laboratory- and synchrotron-based characterization techniques to determine their structure and composition, particle sizes and morphologies, surface properties, as well as As and Fe redox states. Detailed information on sample preparation to minimize oxidation and on solid characterization can be found in the Supporting Information (Text S-2). Mineralogical changes in the solid phase during the reaction were monitored by X-ray powder diffraction (XRD) using a Bruker D8 powder diffractometer (Cu Kα radiation, λ = 1.5406 Å). The morphology, size, structure, and chemical composition of the final solids (collected after 24 h) were characterized by transmission electron microscopy (TEM) and scanning electron microscopy (SEM). TEM micrographs and selected area electron diffraction (SAED) patterns were recorded using a FEI Tecnai G2 F20 X-Twin FEG TEM, operated at 200 keV and equipped with a Gatan Imaging Filter (GIF) Tridiem. SEM images were acquired using a ZEISS Ultra Plus FE-SEM operated in high vacuum mode at an acceleration voltage of 3 kV with 10 μm aperture size using an InLens secondary electron detector. The local structure was investigated using pair distribution function (PDF) analysis. The high energy X-ray scattering data used for PDF analysis were collected at the 11-ID-B beamline of the Advanced Photon Source (Argonne National Laboratory, USA). X-ray absorption spectroscopic (XAS) analyses were carried out to monitor the changes in As oxidation state and to quantify the Fe phases in the final solids. Fe K-edge extended X-ray absorption fine structure (EXAFS) spectra were collected at the SUL-X beamline of Angströmquelle Karlsruhe (ANKA, Karlsruhe, Germany), and the As K-edge X-ray absorption near-edge structure (XANES) data were collected at the BM23 beamline of the European Synchrotron Radiation Facility (ESRF, Grenoble, France). The Fe K-edge EXAFS spectra of synthetic iron (oxyhydr)oxide mineral samples [i.e., FH,[42] GT,[42,43] LP,[42] GR sulfate (GR_{SO4})[33]] were also collected as reference standards for Fe phase quantification. As K-edge XANES spectra of As(III)- and As(V)-interacted GT samples were also collected and were used as reference standards for the determination of As oxidation state.

DOI: 10.1021/acsearthspacechem.9b00031
ACS Earth Space Chem. 2019, 3, 884−894

Table 1. Arsenic Oxidation State and Mineralogical Composition of the End-Products of As(V)-Bearing FH Transformation with Varying $Fe^{2+}_{(aq)}/Fe(III)_{solid}$ Ratios (R)

	As oxidation state			Fe phase composition							
	As K-edge XANES			Fe−K edge EXAFS				PDF			
ratio	As(III)	As(V)	red. χ^2	FH	GT	GR	red. χ^2	FH	GT	GR	goodness of fit (R_w)
0	4.1 ± 0.1	95.9 ± 0.1	0.001	100				100			0.208
0.5	33.6 ± 1.8	66.4 ± 1.7	0.014	17 ± 4	83 ± 3		0.221	70 ± 3	30 ± 1		0.205
1	34.3 ± 1.8	65.7 ± 1.8	0.015	15 ± 1	85 ± 1		2.663	22 ± 5	78 ± 3		0.150
2	42.4 ± 1.8	57.6 ± 1.7	0.013	11 ± 2	84 ± 2	5 ± 1	0.226		92 ± 3	8 ± 1	0.175

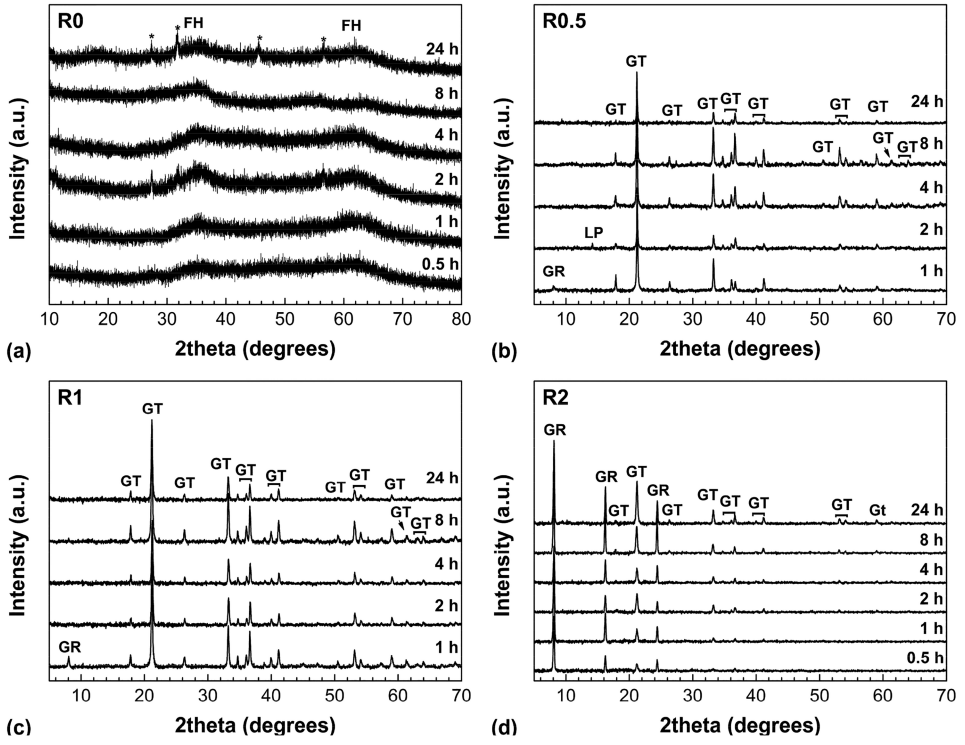

Figure 2. XRD patterns showing the change in mineralogical composition in the solid samples during the 24 h transformation of As(V)-bearing FH at varying $Fe^{2+}_{(aq)}/Fe(III)_{solid}$ ratios (R): (a) control (0), (b) 0.5, (c) 1, and (d) 2. The '*' denotes peaks for halite (NaCl) from the background electrolyte. XRD patterns for R0.5 and R1 at 0.5 h are not shown because no crystalline mineral phases were detected. Note that the increased peak intensity of GR_{SO4} (001) comes from preferential orientation of GR_{SO4} plate-like particles along the [001] zone axis during XRD sample preparation.

X-ray photoelectron spectroscopy (XPS) measurements were performed using a KRATOS Axis Ultra DLD to determine the surface chemistry of the solids. To predict Fe and As speciation and Fe phase stability in the studied system, thermodynamic modeling was carried out using Geochemist's Workbench (GWB)[44] with the MINTEQ thermodynamic database (see Supporting Information Text S-2 for details). Missing thermodynamic data of mineral phases in the Fe−S−H_2O system (e.g., GR_{SO4}) were manually added to the MINTEQ database.[45,46]

RESULTS AND DISCUSSION

Aqueous Behavior and Speciation of Mineral-Bound As Species. The aqueous concentrations of As revealed that barely any As was released (<0.15%, Figure S-1) during the Fe^{2+}-induced transformation of As(V)-bearing FH to GT ± GR. This is consistent with the high uptake capacity of synthetic iron (oxyhydr)oxides for As species determined in the adsorption experiments (Figure S-2). Similar minimal As release (<1%) was also reported in previous Fe^{2+}-catalyzed transformation experiments of As(V)-bearing ferrihydrite[39,47] and As(V)/Sb(V)-bearing jarosite.[45,46] Moreover, it has also been shown that As removal efficiencies were even higher in experiments wherein As was coprecipitated with iron (oxyhydr)oxides compared to those adsorbed onto presynthesized iron (oxyhydr)oxides.[39,48,49]

The oxidation state of As associated with the solids after 24 h of reaction as probed by As K-edge XANES (Figure 1a) showed that the initial FH-bound As(V) was partially reduced to As(III) when the initial As(V)-bearing FH reacted with aqueous Fe^{2+} under anoxic conditions. The degree of As(V) reduction slightly increased from 33.6 ± 1.8% to 42.4 ± 1.8% as the $Fe^{2+}_{(aq)}/Fe(III)_{solid}$ ratio increased from 0.5 to 2 (see Table 1). This trend was also confirmed by high-resolution XPS of the final solids (Figure 1b), which showed the presence of a shoulder at a binding energy of ∼44 eV, indicative of As(III) (see Table S-3 for As reference binding energies). Due to the uncertainty of the XPS measurements (see Table S-4), a fully quantitative determination of the As(III) contents was

DOI: 10.1021/acsearthspacechem.9b00031
ACS Earth Space Chem. 2019, 3, 884−894

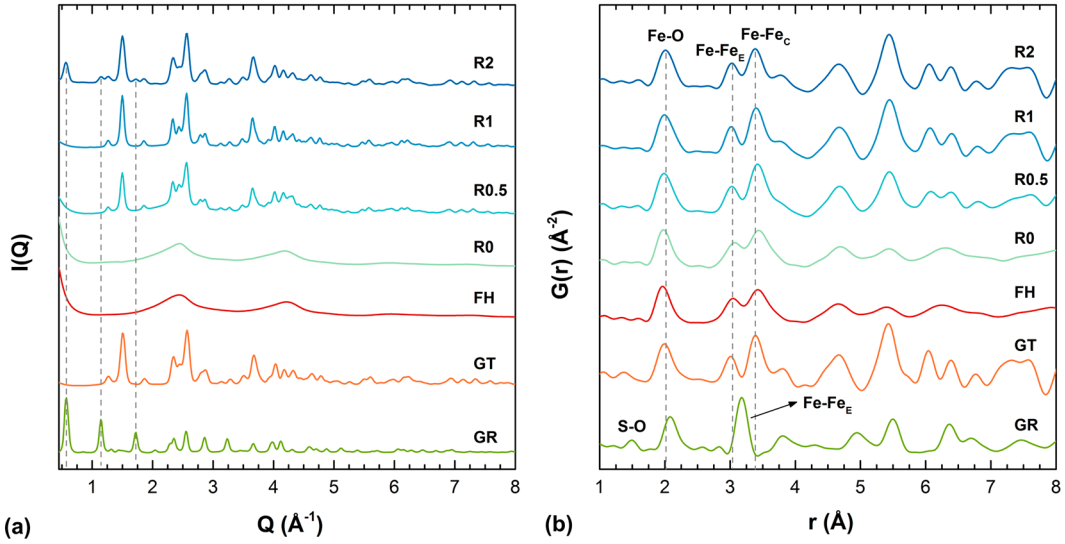

Figure 3. High-energy X-ray scattering data of the end-products after the 24 h transformation of As(V)-bearing FH at varying $Fe^{2+}_{(aq)}/Fe(III)_{solid}$ ratios (R): (a) high-energy XRD patterns [$I(Q)$]. GR (00l) reflections in the R2 end-product are indicated by gray dashed lines, while all the other peaks in the transformation end-products can be assigned to GT (except for the R0 end-product, which is naturally still pure As(V)-bearing FH). The patterns of the reference materials (i.e., FH, GT, and GR) are shown for comparison; and (b) PDFs [$G(r)$] of the low r-value region showing the short-range structure of the solids. The full PDFs are shown in Figure S-4. Fe−Fe_E and Fe−Fe_c refer to edge- and corner-sharing pairs, respectively.

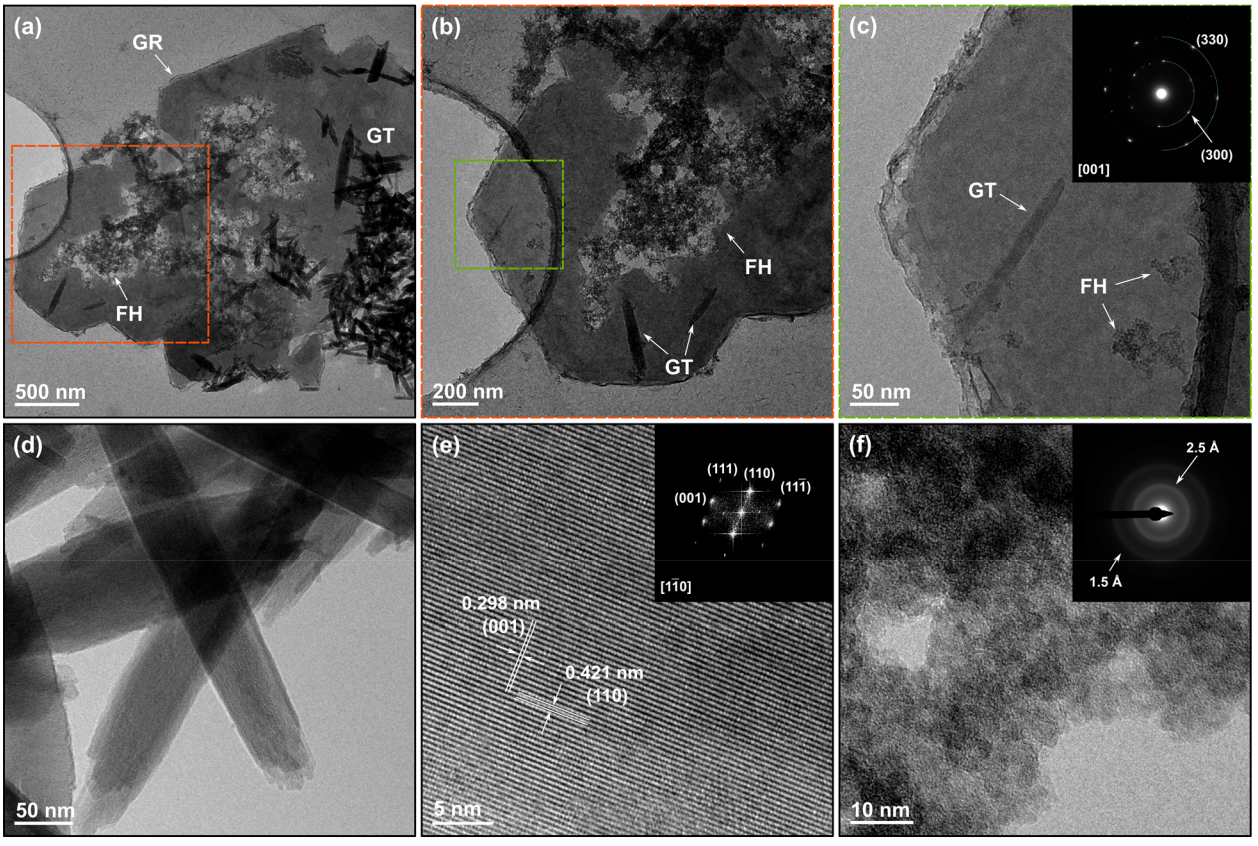

Figure 4. TEM images of Fe phases following the 24 h transformation of As(V)-bearing FH at $Fe^{2+}_{(aq)}/Fe(III)_{solid}$ ratio of 2: (a) overview showing the close association between GR_{SO4} (dark gray, >300 nm wide hexagonal platelets), GT (ca. 50 nm wide black rods), and unreacted FH (aggregates of ∼3 nm sized particles); (b) blow-up of the orange marked area in (a); (c) GR_{SO4} particle seen in green marked area in (b) with the SAED pattern in inset; (d) GT nanorods and the corresponding (e) HRTEM image with the fast Fourier transformation (FFT) pattern in the inset showing the lattice fringes for (001) and (110) planes of GT (in *Pbnm* spacegroup); (f) As(V)-bearing FH nanoparticles with the SAED pattern in the inset. The SAED pattern of GR_{SO4} was indexed according to the proposed structure of Christiansen et al.[56]

DOI: 10.1021/acsearthspacechem.9b00031
ACS Earth Space Chem. 2019, 3, 884−894

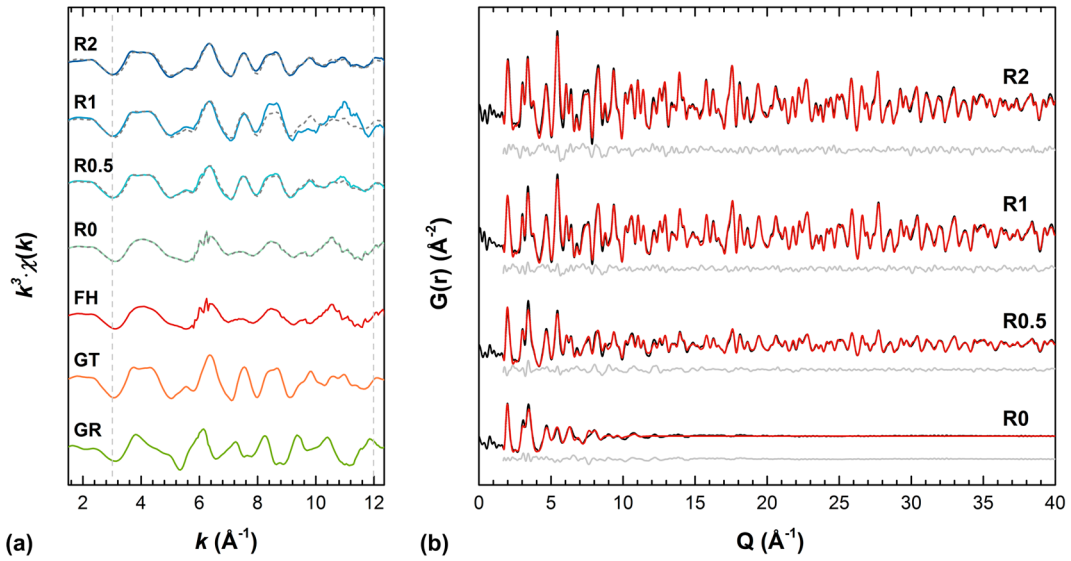

Figure 5. (a) k^3-weighted $\chi(k)$ Fe K-edge EXAFS spectra of transformation end-products following the 24 h transformation of As(V)-bearing FH with varying $Fe^{2+}_{(aq)}$ concentrations ($Fe^{2+}_{(aq)}/Fe(III)_{solid}$ ratios from 0 to 2). Fits (gray dashed lines) are least-squares linear combinations of the reference materials (i.e., lower three patterns FH, GT, and GR_{SO4}). Fit boundaries are indicated by the vertical dashed lines (k-range = 3−12 Å^{-1}). (b) Fits of PDFs of same end-products ($Fe^{2+}_{(aq)}/Fe(III)_{solid}$ ratio from 0 to 2). The black curves represent the experimental data, whereas red and light gray curves represent the calculated pattern and the residuals. Details of the fitting method for Fe K-edge EXAFS and PDF conducted in Athena[57] and PDFgui[58] can be found in Supporting Information Text S-9.

difficult, but XPS confirmed its presence. Furthermore, XPS analyses showed that the initial As(V) was still the primary valence state in the near surface region (top 10 nm of the samples). A possible reduction of As(V) due to X-ray beam damage is negligible as shown by analysis of the control (R0).

Thermodynamic calculations based on the Eh-pH conditions used in our experiments (Figure S-3) suggest that, at equilibrium, all initially adsorbed As(V) species should have been reduced to As(III) during the transformation. The partial reduction of As(V) to As(III) after 24 h observed in our data is likely a result of kinetic limitations since it might take longer time scales for full reduction.

Mineralogical Transformation of As(V)-Bearing FH. In the absence of aqueous Fe^{2+}, the As(V)-bearing FH did not transform to other iron (oxyhydr)oxides (R0, Figure 2a). While barely any As was released during the reactions, exposure of the initial As(V)-bearing FH to varying aqueous Fe^{2+} concentrations led to its rapid transformation into more crystalline iron (oxyhydr)oxides. At $Fe^{2+}_{(aq)}/Fe(III)_{solid}$ ratios of 0.5 and 1 (R0.5 and R1, Figure 2b,c, respectively), goethite (GT) formed within the first hour and dominated the pattern over the remaining 24 h. Small amounts of green rust sulfate (GR_{SO4}) and lepidocrocite (LP, only in R0.5) also formed in the R0.5 and R1 experiments. However, both phases dissolved, as supported by aqueous Fe^{2+} release (Figure S-1), which then precipitated as goethite after 2 h. At an $Fe^{2+}_{(aq)}/Fe(III)_{solid}$ ratio of 2 (R2, Figure 2d), both GT and GR_{SO4} formed rapidly within the first 30 min but both also remained present throughout the 24 h of reaction.

The high energy XRD pattern [$I(Q)$] of the mineral end-products (Figure 3a) corroborated the laboratory-based XRD data (Figure 2), with the main end-product being GT and with some GR_{SO4} forming at the highest tested $Fe^{2+}_{(aq)}/Fe(III)_{solid}$ ratio of 2. The broad humps at Q-values of ∼2.4 and ∼4.2 Å^{-1} for R0.5 and, in part, R1 stem from unreacted FH, the presence of which was not unexpected in the end-product material because previous studies[50−52] have shown that As can slow down the transformation of FH to crystalline iron (oxyhydr)-oxides. The PDF analyses (Figures 3b and S-4) were used to derive the characteristic interatomic distances in the mineral-end products. The atomic pair correlations at r-values < 4 Å (Figure 3b) correspond to the atomic arrangements in the Fe−O polyhedra in iron (oxyhydr)oxides. The first peak at ∼2.0 Å matches first neighbor Fe−O pairs, while peaks at ∼3.0 and ∼3.4 Å represent edge- and corner-sharing Fe−Fe pairs ($Fe-Fe_E$, $Fe-Fe_C$), respectively. Changes in peak positions and intensities for these Fe−Fe pairs are a consequence of the presence of mixed iron (oxyhydr)oxides (i.e., GT, FH ± GR_{SO4}) in these solids, when compared with the standard materials (spectra labeled GT, FH, and GR in Figure 3a,b).

TEM and SEM analyses of the transformation end-products confirmed that GT was the main product with FH still present in all experiments after 24 h. As shown before with XRD and PDF, GR_{SO4} was only present in reactions with $Fe^{2+}_{(aq)}/Fe(III)_{solid}$ = 2 (Figures 4a, S-5, and S-6). GR_{SO4} was identified by its thin hexagonal plate-like particles (Figure 4b),[33,53,54] GT by its distinctive crystalline nanorod (Figure 4d), and FH by its ∼3 nm-sized particle aggregates (Figures 4f and S-5). SEM images of the end-products also revealed that particle lengths of the GT nanorods gradually decreased with increasing $Fe^{2+}_{(aq)}/Fe(III)_{solid}$ ratios (Figures S-6 and S-7). Both TEM and SEM images confirmed that GT was the dominant mineral phase in all experiments (Figures 4a, S-5, and S-6) and that FH was closely associated with GT and GR_{SO4} (Figure 4a,b). It is important to note that, often, FH was observed to seemingly "fill" voids in GR_{SO4} particles (Figures 4a,b and S-5c). Such features could indicate that the GR_{SO4} particles were still forming from the As(V)-bearing FH precursor after 24 h, or that the formed GR_{SO4} crystals are dissolving from the center, as previously suggested by Skovbjerg et al.[55] However, dissolution of the GR_{SO4} from the exposed crystal edges (Figure 4c) cannot be excluded.

DOI: 10.1021/acsearthspacechem.9b00031
ACS Earth Space Chem. 2019, 3, 884−894

From the evaluation of the Fe K-edge EXAFS and PDF data (Figure 5, Table 1), we determined the relative amounts (% mol Fe) of the reaction transformation end-products. The Fe K-edge EXAFS data (Figure 5a) confirmed GT (≥84%) as the main mineral phase in all Fe^{2+}-spiked experiments, with GR only accounting for ∼5% in the system with $Fe^{2+}_{(aq)}/Fe(III)_{solid}$ = 2. The EXAFS fitting revealed that the amount of remnant As(V)-FH after 24 h was inversely proportional to the Fe^{2+} concentration added to the As(V)-bearing FH. Interestingly, the amount of As(V)-FH derived from the PDF data (Figure 5b) followed a similar trend to the EXAFS data, but unreacted FH could not be identified in the R2 end-product PDF pattern. This was most likely due to its low relative amount in the sample (from EXAFS ≈ 11%). However, the biggest difference in the relative phase amounts between PDF and EXAFS fitting was seen in the R0.5 end-product. PDF indicates ∼70% FH compared to ∼16% from the EXAFS evaluation, which naturally also impacted the proportion of GT in this sample. Upon closer inspection, PDF of the R0.5 end-product (Figure 3b) seems to lack the characteristic GT features observed in R1 and R2 samples. For example, the small but sharp peak at r ≈ 3.8 Å is missing, and both the peak at 5.5 Å and the double peaks at 6−6.5 Å are also poorly developed. Thus, the bonding environment at ∼3.8 to ∼7 Å does not exactly resemble GT. From this, we suspect that there is a short-range distortion in the Fe octahedra that is uncharacteristic of GT. This results in the large discrepancy between the PDF and EXAFS Fe phase quantification. Despite the variation between the calculated proportions of Fe phases from EXAFS and PDF data, and considering both experimental, analytical, and fitting uncertainties, the results show that both the extent of FH transformation to GT and/or GR increases as the $Fe^{2+}_{(aq)}/Fe(III)_{solid}$ ratios increase.[27]

Overall, the compositions of the mineral end-products as determined with XRD, PDF, TEM, SEM, and EXAFS at the end of the 24-h Fe^{2+}-induced As(V)-bearing FH transformation are consistent with each other and also match the predicted phases from thermodynamic calculations for the Fe−S−H_2O system (Figure S-8).

Mechanism of As(V)-Ferrihydrite Transformation and As Redox Transformation. Iron redox cycling in subsurface environments highly impacts the mobility and toxicity of As in contaminated sediments and groundwaters. Specifically, mineral transformations involving iron (oxyhydr)oxides are important since, especially under reducing conditions, such transformation reactions can change the oxidation state of mineral-associated As, which in turn controls As toxicity as well as the extent to which As will be sorbed by minerals. Thus, such reactions may not only release As back into the environment, but these processes could render As to be present in the more toxic form.

Our results demonstrated that the initial As(V)-bearing FH rapidly transforms to GT and to a lesser extent to GR_{SO4} and lepidocrocite upon the addition of Fe^{2+} (Figure 2). We also showed that the transformation rate of FH increased with increasing $Fe^{2+}_{(aq)}/Fe(III)_{solid}$ ratios. This is seen, for example, by the appearance of crystalline Fe phases already after 30 min in experiments with an $Fe^{2+}_{(aq)}/Fe(III)_{solid}$ ratio of 2 (Figure 2d), compared to 1 h at lower ratios or in the lower relative abundance of FH in the end-products at higher $Fe^{2+}_{(aq)}/Fe(III)_{solid}$ ratios (Figure 5). Furthermore, the absence of LP at $Fe^{2+}_{(aq)}/Fe(III)_{solid}$ ratios >0.5 indicates that the transformation was very fast because LP formation requires low levels of FH-surface-adsorbed Fe^{2+}.[17,39,45] Moreover, the smaller GT nanorods obtained at higher $Fe^{2+}_{(aq)}/Fe(III)_{solid}$ ratios (Figure S-6) indicate faster FH transformation rates because higher nucleation rates lead to smaller crystals.

GR_{SO4} formed under all tested conditions alongside with GT, but disappeared already after 2 h at lower $Fe^{2+}_{(aq)}/Fe(III)_{solid}$ ratios (<2), and it transformed into the thermodynamically more stable GT (Figure 2b,c). At $Fe^{2+}_{(aq)}/Fe(III)_{solid}$ = 2, GR_{SO4} remained throughout the reaction as expected based on previous Fe^{2+}-induced FH transformation experiments where a similar $Fe^{2+}_{(aq)}/Fe(III)_{solid}$ ratio was employed without the addition of As.[28,29,59] However, in contrast to the As-free FH experiments, which only formed GR, the R2 end-products in the current study also contained FH and GT. Arsenic species have been shown to hinder iron (oxyhydr)oxide transformations.[30,45,60] Thus, the incomplete conversion of As(V)-bearing FH into GT and/or GR_{SO4} (Figures 4 and 5) is likely a consequence of crystallite poisoning by the surface-bound As species. Specifically, As species have been shown to inhibit Fe−O−Fe polymerization, thereby inducing distortions in the Fe bonding environment and inhibiting crystal nucleation and growth.[50−52]

The solid-state characterization results and electron microscopy images further suggest that GR_{SO4} formed independently of GT during the Fe^{2+}-induced transformation of As(V)-bearing FH. The XRD data (Figure 2) document the rapid and simultaneous occurrence of GT and GR_{SO4} in the early stages of transformation and thus suggest that both Fe phases formed directly from FH. This is also supported by the calculated Gibbs free energies ($\Delta G_{rxn}°$), which showed that the formation of GR_{SO4} is more thermodynamically favored from a FH precursor (Table 2, eq 2) compared to GT (Table 2, eq 3). Moreover, the added Fe^{2+} rapidly hydrolyzed, as evidenced by

Table 2. Calculated Gibbs Free Energies ($\Delta G_r°$) at 25 °C

	chemical reaction	$\Delta G_{rxn}°$ (kJ mol^{-1})[a]
	Mineral Formation	
1	$Fe^{III}(OH)_3 \rightarrow \alpha\text{-}Fe^{III}OOH + H_2O$	−20.4
2	$4Fe^{2+} + 2Fe^{III}(OH)_3 + SO_4^{2-} + 6H_2O \rightarrow Fe^{II}_4Fe^{III}_2(OH)_{12}SO_4 + 6H^+$	124.2
3	$4Fe^{2+} + 2\alpha\text{-}Fe^{III}OOH + SO_4^{2-} + 8H_2O \rightarrow Fe^{II}_4Fe^{III}_2(OH)_{12}SO_4 + 6H^+$	598.4
	Redox Reactions	
4	$Fe^{II}_4Fe^{III}_2(OH)_{12}SO_4 + 2H_2As^{V}O_4^- \rightleftharpoons 6\alpha\text{-}Fe^{III}OOH + 2As^{III}(OH)_3 + SO_4^{2-} + 2H_2O$	−122.2
5	$Fe^{II}_4Fe^{III}_2(OH)_{12}SO_4 + 2HAs^{V}O_4^{2-} + 2H^+ \rightleftharpoons 6\alpha\text{-}Fe^{III}OOH + 2As^{III}(OH)_3 + SO_4^{2-} + 2H_2O$	−202.0
6	$Fe^{II}_4Fe^{III}_2(OH)_{12}SO_4 + 2H_2As^{V}O_4^- + 4H_2O \rightleftharpoons 6Fe^{III}(OH)_3 + 2As^{III}(OH)_3 + SO_4^{2-}$	0.2
7	$Fe^{II}_4Fe^{III}_2(OH)_{12}SO_4 + 2HAs^{V}O_4^{2-} + 4H_2O + 2H^+ \rightleftharpoons 6Fe^{III}(OH)_3 + 2As^{III}(OH)_3 + SO_4^{2-}$	−79.6
8	$2Fe^{2+} + H_2As^{V}O_4^- + 3H_2O \rightleftharpoons 2\alpha\text{-}Fe^{III}OOH + As^{III}(OH)_3 + 3H^+$	21.4
9	$2Fe^{2+} + HAs^{V}O_4^{2-} + 3H_2O \rightleftharpoons 2\alpha\text{-}Fe^{III}OOH + As^{III}(OH)_3 + 2H^+$	−18.5
10	$2Fe^{2+} + H_2As^{V}O_4^- + 5H_2O \rightleftharpoons 2Fe^{III}(OH)_3 + As^{III}(OH)_3 + 3H^+$	62.2
11	$2Fe^{2+} + HAs^{V}O_4^{2-} + 3H_2O \rightleftharpoons 2Fe^{III}(OH)_3 + As^{III}(OH)_3 + 2H^+$	22.3
12	$2Fe^{2+} + H_2As^{V}O_4^- + 3H^+ \rightleftharpoons 2Fe^{3+} + As^{III}(OH)_3 + H_2O$	23.2
13	$2Fe^{2+} + HAs^{V}O_4^{2-} + 4H^+ \rightleftharpoons 2Fe^{3+} + As^{III}(OH)_3 + H_2O$	−16.7

[a]Values calculated from the standard Gibbs free energies ($\Delta G_f°$) of minerals and aqueous species (Table S-6).

DOI: 10.1021/acsearthspacechem.9b00031
ACS Earth Space Chem. 2019, 3, 884−894

the quick decrease in aqueous Fe^{2+} concentration (Figure S-1a), and thus the simultaneous formation of GT and GR_{SO4} from FH is likely. The formation of GT from FH is well documented,[24,27,61] while the formation pathways and mechanisms of GR phases from other iron (oxyhydr)oxides are far less studied.[28,59] Sumoondur et al.,[29] however, reported a similar observation wherein GR_{SO4} formed directly from pure FH (no As added, $Fe^{2+}_{(aq)}/Fe(III)_{solid}$ ratios of 0.5 to 2) within the first 10 min of the Fe^{2+}-catalyzed transformation reaction as monitored by synchrotron-based *in situ* time-resolved energy dispersive X-ray diffraction.

During the transformation reaction of the As(V)-bearing FH a minor initial release of As (<0.15%, Figure S-1b) from its surface was observed. The initial As release is a result of the dissolution of FH, which can have surface areas up to 850 $m^2 g^{-1}$,[3] and the formation of GT and GR phases, which both have lower surface areas. This released As was quickly adsorbed by the newly formed GT and/or GR particles (Figure S-1b). However, the possibility of incorporation of As into the structure of GT cannot be ruled out, especially since the ionic radius of As(V) is similar to tetrahedrally coordinated Fe,[1] although such phenomenon has not yet been documented.[39]

A more relevant finding of this study is that the initial As(V) was partially reduced to As(III) during the Fe^{2+}-induced transformation of As(V)-bearing FH, and this reduction (i.e., As(III)/As(V) ratio) increased with increasing $Fe^{2+}_{(aq)}/Fe(III)_{solid}$ ratio. Based on the calculated $\Delta G_{rxn}°$ values (Table 2, eqs 4−7), the most thermodynamically feasible reductant in the Fe−As−S−H_2O system is GR_{SO4}, yet no study to date has been able to document such reduction of As(V) to As(III) by GR.[41,62,63] Moreover, the formation and stability of the GR in the experiments R0.5 and R1 were substantially lower compared to the R2 experiment (Figure 2). This suggests that another redox couple may have induced As(V) reduction. The most likely candidate is the surface-associated Fe^{2+} and GT redox couple (Table 2, eqs 8−9), which has been shown to reduce other groundwater contaminants such as carbon tetrachloride,[64] nitrobenzene,[65,66] and chromate.[67] The surface-associated Fe^{2+}-GT redox couple might also explain why As(V) reduction was only observed at high Fe^{2+} concentrations during the Fe^{2+}-catalyzed transformation of As(V)/Sb(V)-jarosite ($[Fe(III)_{jarosite}$ = 21.8 mM, $[Fe^{2+}_{(aq)}]$ = 0 to 20 mM, As/Fe_{solid} = 0.003).[45] These authors noted that, in their experiments, LP was the dominant mineral phase at low Fe^{2+} concentrations, while GT was the primary end-product (with minor GR_{SO4}, <10%) at higher Fe^{2+} concentrations.

It must be noted, however, that As(V) reduction has not been observed previously upon interaction with Fe^{2+}-activated synthetic GT (e.g., Amstaetter et al.[68]), who examined the interactions at a $Fe^{2+}_{(aq)}/Fe(III)_{solid}$ ratio of 0.03, which is approximately 15 to 55 times lower than the ratios used in this study. Since the reduction reaction is driven by Fe^{2+} concentration, the low Fe^{2+} concentration used in their study could explain why they did not observe any As(V) reduction to As(III) in their system. However, a question arises whether As(V) could be reduced to As(III) at lower $Fe^{2+}_{(aq)}/Fe(III)_{solid}$ ratios and $Fe(III)_{FH}$ loadings similar to those reported by Pedersen et al.[39] and Masue-Slowey et al.,[40] especially since the mineralogical composition of the end-products is different from what we observed in our study.

Overall, these redox transformations have important implications for the mobility and toxicity of As. The partial reduction of As(V) to As(III), as documented in this study, is an unexpected and also detrimental consequence as such reduction results in the generation of far more toxic and mobile As species.[69] On the positive side, the sorption capacities of these Fe mineral phases toward As species is very high, and therefore, we observed no significant As release. Noteworthy, however, is the fact that invariably real subsurface environments are significantly more complex. The presence of many different mineral substrates and the variation in mineral sorption capacities will be affected by Eh/pH conditions[70] and the presence of other inorganic ions[33,69] (e.g., silicate and phosphate anions) or organic ligands[71−74] all competing with As for active surface sites and influencing the mechanisms and pathways of Fe (oxyhydr)oxide transformation.

CONCLUSION

In subsurface environments, iron-bearing mineral transformations can massively impact the mobility and toxicity of contaminants since these mineral phases serve as toxic element sinks that can control and even prevent release and further transport contaminants in soils and groundwaters. In this study, we followed the transformation of As(V)-bearing ferrihydrite, catalyzed by aqueous Fe^{2+}, under anoxic conditions as it converts to more crystalline iron (oxyhydr)-oxides. Higher Fe^{2+} concentrations resulted in the formation of both GT and GR phases, while lower Fe^{2+} concentrations led to a GT end-product. However, at all the tested conditions, the conversion of ferrihydrite was incomplete, and our data indicate that this was a consequence of As surface complexation. Analyses of the mineral-bound As species also revealed partial reduction of initial As(V) to As(III), although no significant release of As was observed during the transformation. Overall, our results highlight the need to understand such intertransformations among iron (oxyhydr)oxide in subsurface environments where aqueous Fe^{2+} is present as it will impact As sequestration, mobilization, and transport.

ASSOCIATED CONTENT

Supporting Information

The Supporting Information is available free of charge on the ACS Publications website at DOI: 10.1021/acsearthspacechem.9b00031.

Detailed information on mineral characterization and analytical techniques, additional mineral characterization data (TEM, SEM, XAS, PDF), XPS reference data, and thermodynamic calculations (PDF)

AUTHOR INFORMATION

Corresponding Author

*E-mail: jpperez@gfz-potsdam.de.

ORCID

Jeffrey Paulo H. Perez: 0000-0002-0256-0576
Dominique J. Tobler: 0000-0001-8532-1855
Jörg Radnik: 0000-0003-0302-6815

Funding

This project has received funding from the European Union's Horizon 2020 Marie Skłodowska-Curie Innovative Training Network Grant No. 675219. L.G.B. and H.M.F. acknowledge the financial support from the Helmholtz Recruiting Initiative (award number I-044-16-01). Use of the Advanced Photon Source was supported by the U.S. Department of Energy,

DOI: 10.1021/acsearthspacechem.9b00031
ACS Earth Space Chem. 2019, 3, 884−894

Office of Science, Office of Basic Energy Sciences, under Contract No. DE-AC02-06CH11357. D.J.T. and K.D. acknowledge financial support from the Danish Council for Independent Research (via DANSCATT) for travel to APS.

Notes

The authors declare no competing financial interest.

■ ACKNOWLEDGMENTS

ICP-OES analyses were carried out at the Helmholtz Laboratory for the Geochemistry of the Earth Surface (HELGES) at GFZ Potsdam. The authors would like to thank David Uhlig of HELGES for his help during ICP-OES analyses of some of the samples and Sathish Mayana of Interface Geochemistry group at GFZ Potsdam for his help during SEM imaging. J.P.H.P. and A.N.T. thank ANKA for access to SUL-X beamline and beamline staff Jörg Göttlicher and Ralf Steininger for their competent support and advice during collection of Fe K-edge EXAFS data. The As K-edge XANES data were collected at the BM23 beamline at ESRF (experiment no. EV-338), and J.P.H.P., L.G.B., D.J.T., and K.D. thank Sakura Pascarelli for assistance during beamtime. D.J.T. and K.D. thank Olaf Borkiewicz and Kevin A. Beyer for support with X-ray total scattering measurements at APS beamline 11 ID-B, Argonne, USA. J.P.H.P. acknowledges the help of Case Van Genuchten and Hongyan Wang during the XAS beamtime experiments. J.P.H.P. would also like to thank Leonard Daniël Samson for his help with the statistical analysis of the particle size distribution data.

■ REFERENCES

(1) Cornell, R. M.; Schwertmann, U. *The Iron Oxides: Structure, Properties, Reactions, Occurrences and Uses*, 2nd ed.; Wiley-VCH Verlag GmbH & Co. KGaA: Weinheim, FRG, 2003.

(2) Karimian, N.; Johnston, S. G.; Burton, E. D. Iron and sulfur cycling in acid sulfate soil wetlands under dynamic redox conditions: A review. *Chemosphere* **2018**, *197*, 803−816.

(3) Jambor, J. L.; Dutrizac, J. E. Occurrence and constitution of natural and synthetic ferrihydrite, a widespread iron oxyhydroxide. *Chem. Rev.* **1998**, *98* (7), 2549−2586.

(4) Cornell, R. M. The influence of some divalent cations on the transformation of ferrihydrite to more crystalline products. *Clay Miner.* **1988**, *23* (3), 329−332.

(5) Vu, H. P.; Shaw, S.; Brinza, L.; Benning, L. G. Crystallization of hematite (α-Fe_2O_3) under alkaline condition: The effects of Pb. *Cryst. Growth Des.* **2010**, *10* (4), 1544−1551.

(6) Vu, H. P.; Shaw, S.; Brinza, L.; Benning, L. G. Partitioning of Pb(II) during goethite and hematite crystallization: Implications for Pb transport in natural systems. *Appl. Geochem.* **2013**, *39*, 119−128.

(7) Brinza, L.; Vu, H. P.; Shaw, S.; Mosselmans, J. F. W.; Benning, L. G. Effect of Mo and V on the hydrothermal crystallization of hematite from ferrihydrite: An *in situ* energy dispersive X-ray diffraction and X-ray absorption spectroscopy study. *Cryst. Growth Des.* **2015**, *15* (10), 4768−4780.

(8) Brinza, L.; Vu, H. P.; Neamtu, M.; Benning, L. G. Experimental and simulation results of the adsorption of Mo and V onto ferrihydrite. *Sci. Rep.* **2019**, *9* (1), 1365.

(9) Schwertmann, U.; Stanjek, H.; Becher, H. H. Long-term in vitro transformation of 2-line ferrihydrite to goethite/hematite at 4, 10, 15 and 25 °C. *Clay Miner.* **2004**, *39* (4), 433−438.

(10) Schwertmann, U.; Murad, E. Effect of pH on the formation of goethite and hematite from ferrihydrite. *Clays Clay Miner.* **1983**, *31* (4), 277−284.

(11) Das, S.; Hendry, M. J.; Essilfie-Dughan, J. Transformation of two-line ferrihydrite to goethite and hematite as a function of pH and temperature. *Environ. Sci. Technol.* **2011**, *45* (1), 268−275.

(12) Shaw, S.; Pepper, S. E.; Bryan, N. D.; Livens, F. R. The kinetics and mechanisms of goethite and hematite crystallization under alkaline conditions, and in the presence of phosphate. *Am. Mineral.* **2005**, *90* (11−12), 1852−1860.

(13) Jang, J.-H.; Dempsey, B. A.; Catchen, G. L.; Burgos, W. D. Effects of Zn(II), Cu(II), Mn(II), Fe(II), NO_3^-, or SO_4^{2-} at pH 6.5 and 8.5 on transformations of hydrous ferric oxide (HFO) as evidenced by Mössbauer spectroscopy. *Colloids Surf., A* **2003**, *221* (1), 55−68.

(14) Vempati, R.; Loeppert, R. H. Influence of structural and adsorbed Si on the transformation of synthetic ferrihydrite. *Clays Clay Miner.* **1989**, *37* (3), 273−279.

(15) Cornell, R. M.; Schneider, W. Formation of goethite from ferrihydrite at physiological pH under the influence of cysteine. *Polyhedron* **1989**, *8* (2), 149−155.

(16) Cornell, R. M. Comparison and classification of the effects of simple ions and molecules upon the transformation of ferrihydrite into more crystalline products. *Z. Pflanzenernaehr. Bodenkd.* **1987**, *150* (5), 304−307.

(17) Hansel, C. M.; Benner, S. G.; Fendorf, S. Competing Fe(II)-induced mineralization pathways of ferrihydrite. *Environ. Sci. Technol.* **2005**, *39* (18), 7147−7153.

(18) Tronc, E.; Belleville, P.; Jolivet, J. P.; Livage, J. Transformation of ferric hydroxide into spinel by iron(II) adsorption. *Langmuir* **1992**, *8* (1), 313−319.

(19) Liu, H.; Li, P.; Zhu, M.; Wei, Y.; Sun, Y. Fe(II)-induced transformation from ferrihydrite to lepidocrocite and goethite. *J. Solid State Chem.* **2007**, *180* (7), 2121−2128.

(20) Yang, L.; Steefel, C. I.; Marcus, M. A.; Bargar, J. R. Kinetics of Fe(II)-catalyzed transformation of 6-line ferrihydrite under anaerobic flow conditions. *Environ. Sci. Technol.* **2010**, *44* (14), 5469−5475.

(21) Kappler, A.; Straub, K. L. Geomicrobiological cycling of iron. *Reviews in Mineralogy and Geochemistry* **2005**, *59* (1), 85−108.

(22) Fortin, D.; Langley, S. Formation and occurrence of biogenic iron-rich minerals. *Earth-Sci. Rev.* **2005**, *72* (1), 1−19.

(23) Hiemstra, T.; van Riemsdijk, W. H. Adsorption and surface oxidation of Fe(II) on metal (hydr)oxides. *Geochim. Cosmochim. Acta* **2007**, *71* (24), 5913−5933.

(24) Gorski, C. A.; Scherer, M. M. Fe^{2+} sorption at the Fe oxide-water interface: A revised conceptual framework. In *Aquatic Redox Chemistry*; Tratnyek, P. G., Grundl, T. J., Haderlein, S. B., Eds.; American Chemical Society: 2011; Vol. *1071*, pp 315−343.

(25) Katz, J. E.; Zhang, X.; Attenkofer, K.; Chapman, K. W.; Frandsen, C.; Zarzycki, P.; Rosso, K. M.; Falcone, R. W.; Waychunas, G. A.; Gilbert, B. Electron small polarons and their mobility in iron (oxyhydr)oxide nanoparticles. *Science* **2012**, *337* (6099), 1200−1203.

(26) Williams, A. G. B.; Scherer, M. M. Spectroscopic evidence for Fe(II)−Fe(III) electron transfer at the iron oxide−water interface. *Environ. Sci. Technol.* **2004**, *38* (18), 4782−4790.

(27) Boland, D. D.; Collins, R. N.; Miller, C. J.; Glover, C. J.; Waite, T. D. Effect of solution and solid-phase conditions on the Fe(II)-accelerated transformation of ferrihydrite to lepidocrocite and goethite. *Environ. Sci. Technol.* **2014**, *48* (10), 5477−5485.

(28) Ahmed, I. A. M.; Benning, L. G.; Kakonyi, G.; Sumoondur, A. D.; Terrill, N. J.; Shaw, S. Formation of green rust sulfate: A combined *in situ* time-resolved X-ray scattering and electrochemical study. *Langmuir* **2010**, *26* (9), 6593−6603.

(29) Sumoondur, A.; Shaw, S.; Ahmed, I.; Benning, L. G. Green rust as a precursor for magnetite: An *in situ* synchrotron based study. *Mineral. Mag.* **2008**, *72* (1), 201−204.

(30) Wang, Y.; Morin, G.; Ona-Nguema, G.; Brown, G. E. Arsenic(III) and arsenic(V) speciation during transformation of lepidocrocite to magnetite. *Environ. Sci. Technol.* **2014**, *48* (24), 14282−14290.

(31) Vaughan, D. J. Arsenic. *Elements* **2006**, *2* (2), 71−75.

(32) Smedley, P. L.; Kinniburgh, D. G. A review of the source, behaviour and distribution of arsenic in natural waters. *Appl. Geochem.* **2002**, *17* (5), 517−568.

DOI: 10.1021/acsearthspacechem.9b00031
ACS Earth Space Chem. 2019, 3, 884−894

(33) Perez, J. P. H.; Freeman, H. M.; Schuessler, J. A.; Benning, L. G. The interfacial reactivity of arsenic species with green rust sulfate (GR_{SO4}). *Sci. Total Environ.* **2019**, *648*, 1161−1170.
(34) Raven, K. P.; Jain, A.; Loeppert, R. H. Arsenite and arsenate adsorption on ferrihydrite: Kinetics, equilibrium, and adsorption envelopes. *Environ. Sci. Technol.* **1998**, *32* (3), 344−349.
(35) Mamindy-Pajany, Y.; Hurel, C.; Marmier, N.; Roméo, M. Arsenic adsorption onto hematite and goethite. *C. R. Chim.* **2009**, *12* (8), 876−881.
(36) Tang, W.; Li, Q.; Gao, S.; Shang, J. K. Arsenic (III,V) removal from aqueous solution by ultrafine α-Fe_2O_3 nanoparticles synthesized from solvent thermal method. *J. Hazard. Mater.* **2011**, *192* (1), 131−138.
(37) Lin, S.; Lu, D.; Liu, Z. Removal of arsenic contaminants with magnetic γ-Fe_2O_3 nanoparticles. *Chem. Eng. J.* **2012**, *211−212*, 46−52.
(38) Feng, L.; Cao, M.; Ma, X.; Zhu, Y.; Hu, C. Superparamagnetic high-surface-area Fe_3O_4 nanoparticles as adsorbents for arsenic removal. *J. Hazard. Mater.* **2012**, *217−218*, 439−446.
(39) Pedersen, H. D.; Postma, D.; Jakobsen, R. Release of arsenic associated with the reduction and transformation of iron oxides. *Geochim. Cosmochim. Acta* **2006**, *70* (16), 4116−4129.
(40) Masue-Slowey, Y.; Loeppert, R. H.; Fendorf, S. Alteration of ferrihydrite reductive dissolution and transformation by adsorbed As and structural Al: Implications for As retention. *Geochim. Cosmochim. Acta* **2011**, *75* (3), 870−886.
(41) Jönsson, J.; Sherman, D. M. Sorption of As(III) and As(V) to siderite, green rust (fougerite) and magnetite: Implications for arsenic release in anoxic groundwaters. *Chem. Geol.* **2008**, *255* (1−2), 173−181.
(42) Schwertmann, U.; Cornell, R. M. *Iron Oxides in the Laboratory: Preparation and Characterization*, 2nd ed.; Wiley-VCH Verlag GmbH & Co. KGaA: Weinheim, FRG, 2000; p 188.
(43) Atkinson, R. J.; Posner, A. M.; Quirk, J. P. Adsorption of potential-determining ions at the ferric oxide-aqueous electrolyte interface. *J. Phys. Chem.* **1967**, *71* (3), 550−558.
(44) Bethke, C. M. *Geochemical and Biogeochemical Reaction Modeling*; Cambridge University Press: 2010.
(45) Karimian, N.; Johnston, S. G.; Burton, E. D. Antimony and arsenic behavior during Fe(II)-induced transformation of jarosite. *Environ. Sci. Technol.* **2017**, *51* (8), 4259−4268.
(46) Karimian, N.; Johnston, S. G.; Burton, E. D. Antimony and arsenic partitioning during Fe^{2+}-induced transformation of jarosite under acidic conditions. *Chemosphere* **2018**, *195*, 515−523.
(47) Gomez, M. A.; Jim Hendry, M.; Hossain, A.; Das, S.; Elouatik, S. Abiotic reduction of 2-line ferrihydrite: Effects on adsorbed arsenate, molybdate, and nickel. *RSC Adv.* **2013**, *3* (48), 25812−25822.
(48) Asta, M. P.; Cama, J.; Martínez, M.; Giménez, J. Arsenic removal by goethite and jarosite in acidic conditions and its environmental implications. *J. Hazard. Mater.* **2009**, *171* (1), 965−972.
(49) Park, J. H.; Han, Y.-S.; Ahn, J. S. Comparison of arsenic co-precipitation and adsorption by iron minerals and the mechanism of arsenic natural attenuation in a mine stream. *Water Res.* **2016**, *106*, 295−303.
(50) Waychunas, G. A.; Rea, B. A.; Fuller, C. C.; Davis, J. A. Surface chemistry of ferrihydrite: Part 1. EXAFS studies of the geometry of coprecipitated and adsorbed arsenate. *Geochim. Cosmochim. Acta* **1993**, *57* (10), 2251−2269.
(51) Richmond, W. R.; Loan, M.; Morton, J.; Parkinson, G. M. Arsenic removal from aqueous solution via ferrihydrite crystallization control. *Environ. Sci. Technol.* **2004**, *38* (8), 2368−2372.
(52) Rancourt, D. G.; Fortin, D.; Pichler, T.; Thibault, P.-J.; Lamarche, G.; Morris, R. V.; Mercier, P. H. J. Mineralogy of a natural As-rich hydrous ferric oxide coprecipitate formed by mixing of hydrothermal fluid and seawater: Implications regarding surface complexation and color banding in ferrihydrite deposits. *Am. Mineral.* **2001**, *86* (7−8), 834−851.
(53) Freeman, H. M.; Perez, J. P. H.; Hondow, N.; Benning, L. G.; Brown, A. P. Beam-induced oxidation of mixed-valent Fe (oxyhydr)-oxides (green rust) monitored by STEM-EELS. *Micron* **2019**, DOI: 10.1016/j.micron.2019.02.002.
(54) Perez, J. P. H.; Mangayayam, M. C.; Rubio, S. N.; Freeman, H. M.; Tobler, D. J.; Benning, L. G. Intercalation of aromatic sulfonates in 'green rust' via ion exchange. *Energy Procedia* **2018**, *146*, 179−187.
(55) Skovbjerg, L. L.; Stipp, S. L. S.; Utsunomiya, S.; Ewing, R. C. The mechanisms of reduction of hexavalent chromium by green rust sodium sulphate: Formation of Cr-goethite. *Geochim. Cosmochim. Acta* **2006**, *70* (14), 3582−3592.
(56) Christiansen, B. C.; Balic-Zunic, T.; Petit, P. O.; Frandsen, C.; Mørup, S.; Geckeis, H.; Katerinopoulou, A.; Stipp, S. L. S. Composition and structure of an iron-bearing, layered double hydroxide (LDH) − Green rust sodium sulphate. *Geochim. Cosmochim. Acta* **2009**, *73* (12), 3579−3592.
(57) Ravel, B.; Newville, M. ATHENA, ARTEMIS, HEPHAESTUS: Data analysis for X-ray absorption spectroscopy using IFEFFIT. *J. Synchrotron Radiat.* **2005**, *12* (4), 537−541.
(58) Farrow, C. L.; Juhas, P.; Liu, J. W.; Bryndin, D.; Božin, E. S.; Bloch, J.; Th, P.; Billinge, S. J. L. PDFfit2 and PDFgui: Computer programs for studying nanostructure in crystals. *J. Phys.: Condens. Matter* **2007**, *19* (33), 335219.
(59) Usman, M.; Hanna, K.; Abdelmoula, M.; Zegeye, A.; Faure, P.; Ruby, C. Formation of green rust via mineralogical transformation of ferric oxides (ferrihydrite, goethite and hematite). *Appl. Clay Sci.* **2012**, *64*, 38−43.
(60) Su, C.; Puls, R. W. Significance of iron(II,III) hydroxycarbonate green rust in arsenic remediation using zerovalent iron in laboratory column tests. *Environ. Sci. Technol.* **2004**, *38* (19), 5224−5231.
(61) Yee, N.; Shaw, S.; Benning, L. G.; Nguyen, T. H. The rate of ferrihydrite transformation to goethite via the Fe(II) pathway. *Am. Mineral.* **2006**, *91* (1), 92−96.
(62) Wang, Y.; Morin, G.; Ona-Nguema, G.; Juillot, F.; Guyot, F.; Calas, G.; Brown, G. E. Evidence for different surface speciation of arsenite and arsenate on green rust: An EXAFS and XANES Study. *Environ. Sci. Technol.* **2010**, *44* (1), 109−115.
(63) Randall, S. R.; Sherman, D. M.; Ragnarsdottir, K. V. Sorption of As(V) on green rust ($Fe_4(II)Fe_2(III)(OH)_{12}SO_4{\cdot}3H_2O$) and lepidocrocite ($\gamma$-FeOOH): Surface complexes from EXAFS spectroscopy. *Geochim. Cosmochim. Acta* **2001**, *65* (7), 1015−1023.
(64) Amonette, J. E.; Workman, D. J.; Kennedy, D. W.; Fruchter, J. S.; Gorby, Y. A. Dechlorination of carbon tetrachloride by Fe(II) associated with goethite. *Environ. Sci. Technol.* **2000**, *34* (21), 4606−4613.
(65) Stewart, S. M.; Hofstetter, T. B.; Joshi, P.; Gorski, C. A. Linking thermodynamics to pollutant reduction kinetics by Fe^{2+} bound to iron oxides. *Environ. Sci. Technol.* **2018**, *52* (10), 5600−5609.
(66) Gorski, C. A.; Edwards, R.; Sander, M.; Hofstetter, T. B.; Stewart, S. M. Thermodynamic characterization of iron oxide−aqueous Fe^{2+} redox couples. *Environ. Sci. Technol.* **2016**, *50* (16), 8538−8547.
(67) Buerge, I. J.; Hug, S. J. Influence of mineral surfaces on chromium(VI) reduction by iron(II). *Environ. Sci. Technol.* **1999**, *33* (23), 4285−4291.
(68) Amstaetter, K.; Borch, T.; Larese-Casanova, P.; Kappler, A. Redox transformation of arsenic by Fe(II)-activated goethite (α-FeOOH). *Environ. Sci. Technol.* **2010**, *44* (1), 102−108.
(69) Roberts, L. C.; Hug, S. J.; Ruettimann, T.; Billah, M. M.; Khan, A. W.; Rahman, M. T. Arsenic removal with iron(II) and iron(III) in waters with high silicate and phosphate concentrations. *Environ. Sci. Technol.* **2004**, *38* (1), 307−315.
(70) Root, R. A.; Dixit, S.; Campbell, K. M.; Jew, A. D.; Hering, J. G.; O'Day, P. A. Arsenic sequestration by sorption processes in high-iron sediments. *Geochim. Cosmochim. Acta* **2007**, *71* (23), 5782−5803.
(71) Zhou, Z.; Latta, D. E.; Noor, N.; Thompson, A.; Borch, T.; Scherer, M. M. Fe(II)-catalyzed transformation of organic matter−

ferrihydrite coprecipitates: A closer look using e isotopes. *Environ. Sci. Technol.* **2018**, *52* (19), 11142−11150.
(72) Chen, C.; Sparks, D. L. Fe(II)-induced mineral transformation of ferrihydrite−organic matter adsorption and co-precipitation complexes in the absence and presence of As(III). *ACS Earth and Space Chemistry* **2018**, *2* (11), 1095−1101.
(73) Chen, C.; Kukkadapu, R.; Sparks, D. L. Influence of coprecipitated organic matter on $Fe^{2+(aq)}$-catalyzed transformation of ferrihydrite: Implications for carbon dynamics. *Environ. Sci. Technol.* **2015**, *49* (18), 10927−10936.
(74) Hu, S.; Lu, Y.; Peng, L.; Wang, P.; Zhu, M.; Dohnalkova, A. C.; Chen, H.; Lin, Z.; Dang, Z.; Shi, Z. Coupled kinetics of ferrihydrite transformation and As(V) sequestration under the effect of humic acids: A mechanistic and quantitative study. *Environ. Sci. Technol.* **2018**, *52* (20), 11632−11641.

DOI: 10.1021/acsearthspacechem.9b00031
ACS Earth Space Chem. 2019, 3, 884−894